Elucidating the critical oligomeric steps in secondary organic aerosol and brown carbon formation

Yuemeng Ji[1,2], Qiuju Shi[1,2], Xiaohui Ma[1,2], Lei Gao[1,2], Jiaxin Wang[1,2], Yixin Li[3], Yanpeng Gao[1,2], Guiying Li[1,2], Renyi Zhang[3], and Taicheng An[1,2]

[1]Guangdong-Hong Kong-Macao Joint Laboratory for Contaminants Exposure and Health, Guangdong Key Laboratory of Environmental Catalysis and Health Risk Control, Institute Environmental Health and Pollution control, Guangdong University of Technology, Guangzhou 510006, China
[2]Guangzhou Key Laboratory of Environmental Catalysis and Pollution Control, Key Laboratory of City Cluster Environmental Safety and Green development (Department of Education), School of Environmental Science and Engineering, Guangdong University of Technology, Guangzhou 510006, China
[3]Department of Atmospheric Sciences, Texas A&M University, College Station, Texas 77843, United States

Correspondence to: Yuemeng Ji (jiym@gdut.edu.cn) and Taicheng An (antc99@gdut.edu.cn)

Abstract. Small α-dicarbonyls represent the major precursors for secondary organic aerosol (SOA) and brown carbon (BrC) in the atmosphere, but the chemical mechanisms leading to their formation remain unclear. Here we elucidate the fundamental kinetics and mechanisms for aqueous-phase oligomerization of glyoxal (GL) using quantum chemical and kinetic rate calculations. Our results identify several essential isomeric processes for GL, including protonation to yield diol/tetrol and carbenium ions, nucleophilic addition of carbenium ions to diol/tetrol as well as to free methylamine/ammonia (MA/AM), and deprotonation to propagate oligomers and N-heterocycles. Both protonation and nucleophilic addition occur without activation barriers and are dominantly driven by electrostatic attraction. Deprotonation proceeds readily via water molecules in the absence of MA/AM but corresponds to the rate-limiting step for N-containing cationic intermediates to yield N-heterocycles. On the other hand, the latter occurs readily via a catalytic process by acidic anions (eg., SO_4^{2-}). A carbenium ion-mediated reaction rate of GL is 4.62×10^{-3} s^{-1} under atmospheric conditions, in good agreement with the experimental data. Our results provide essential mechanistic and kinetic data for accurate assessment of the role of small α-dicarbonyls in SOA and BrC formation.

1 Introduction

Volatile organic compounds (VOCs) from biogenic and anthropogenic sources are of particular importance due to their chemical reactivity and high abundance in the atmosphere (Piccot, 1992; Acosta Navarro et al., 2014). Gas-phase reactions of VOCs associated with photochemical oxidant cycles generally produce secondary organic aerosol (SOA) particle mass and increase tropospheric ozone concentration (Lim et al., 2005; Ziemann and Atkinson, 2012; Wang et al., 2020a; Ge et al., 2021; Wang et al., 2020b; Ma et al., 2021). Hence, the emission of VOCs is a key process in controlling the formation and growth of new particles over continental regions. Oxidation of biogenic terpenes from terrestrial vegetation and aromatics

from human activities generates a large number of organic carbonyls, which are major precursors of SOA (Altieri et al., 2006; Volkamer et al., 2001; Gomez Alvarez et al., 2007; Sareen et al., 2016; Yang et al., 2020). These organic carbonyls engage in a variety of reactions, including new particle formation, condensation/equilibrium partitioning, particle- and aqueous-

35   phase reactions, leading to an additional products formation in the particle phase (Loeffler et al., 2006; Kroll et al., 2005; Nozie`Re et al., 2009; Marrero-Ortiz et al., 2019; Tuguldurova et al., 2019; Kua et al., 2011; Li et al., 2020; Shi et al., 2019; Xia et al., 2021).

Glyoxal (GL), an important and simple carbonyl compound, is originated from the gas-phase oxidation of biogenic isoprene and anthropogenic aromatics (Volkamer et al., 2001; Gomez Alvarez et al., 2007; Lim et al., 2005). The global

40   source of GL is estimated to be 45-56 Tg yr^{-1} (Fu et al., 2008; Myriokefalitakis et al., 2008), with a predicted contribution of 2.6 Tg C yr^{-1} to global SOA mass (Fu et al., 2008). GL and methylglyoxal contribute to 16% of SOA mass during a severe haze episode in Hebei province, China (Li et al., 2021a). In Mexico City, GL contributes at least 15% of SOA mass (Volkamer et al., 2007), and in the Pearl River Delta, China, 21% of SOA formation originates from the heterogeneous reactions of GL and methylglyoxal (Ling et al., 2020). Hence, GL is a primary contributor to the rapid and efficient

45   formation of SOA under urban environments. The aqueous-phase reaction of GL starts with hydration, subsequently forming several high-molecular-weight oligomers, such as dimers, trimers, tetramers, and pentamers (Hastings et al., 2005; Loeffler et al., 2006; Gomez et al., 2015; Kua et al., 2008; Avzianova and Brooks, 2013). Previous theoretical studies have suggested that the direct hydration of GL is thermodynamically and kinetically unfeasible (Shi et al., 2020; Ji et al., 2020). The rapid growth of SOA was observed in sulfuric acid nanoparticles (Jang et al., 2002; Huang et al., 2016; Surratt et al., 2007; Liggio

50   et al., 2005b), while several other studies have revealed little effect of acids (such as sulfuric acid) on the formation of GL oligomers (Loeffler et al., 2006; Kroll et al., 2005). Hence, the aqueous-phase chemical reaction mechanism of GL and its role in SOA formation are still unclear.

On the other hand, brown carbon (BrC) is also generated by the aqueous-phase reaction of GL in the presence of amines or ammonium in the troposphere (Li et al., 2021b; Shapiro et al., 2009; Galloway et al., 2009; Lee et al., 2013; Maxut et al.,

55   2015; Marrero-Ortiz et al., 2019; Tuguldurova et al., 2019; Kua et al., 2011). Zhang and co-workers have revealed a slight browning of glyoxal-amine mixtures (Marrero-Ortiz et al., 2019; Li et al., 2021b). They also have identified oligomers and N-heterocycles in NH$_4$HSO$_4$ and (NH$_4$)$_2$SO$_4$, whereas only oligomers were detected in NaCl (Li et al., 2021b). Shapiro et al. have detected light-absorbing products, slowly formed from GL in mildly acidic salt solution of (NH$_4$)$_2$SO$_4$, using UV/vis spectrophotometry and matrix-assisted laser desorption ionization mass spectrometry (Shapiro et al., 2009). A chamber study

60   of GL uptake to (NH$_4$)$_2$SO$_4$ solution has been performed using a high-resolution time-of-flight aerosol mass spectrometer and found that carbon-nitrogen (C-N) compounds are irreversibly produced in the solution (Galloway et al., 2009). However, De Haan et al. have described a rapid but reversible BrC formation in (NH$_4$)$_2$SO$_4$ droplets in dry condition (RH<5%) using cavity attenuated phase shift single-scattering albedo spectrometry (De Haan et al., 2020). In addition, Powelson et al. have found that the reaction of GL with methylamine is more effective than that with (NH$_4$)$_2$SO$_4$ by using UV-vis and

65   fluorescence spectroscopy (Powelson et al., 2014), while Lian et al. have proven that the synergistic effect of ammonium and

amines contributes to the formation of imidazole in cloud processing (Lian et al., 2020). Most previous studies have shown that imidazole and high-molecular-weight light-absorbing C-N compounds are produced by different atmospheric chemical reactions of GL with amines/ammonium, but the reaction mechanism is yet to be clarified.

In this work, the aqueous-phase chemistry of GL in the absence and presence of methylamine/ammonia (MA/AM) was systematically investigated using quantum chemical calculations. The fundamental chemical mechanisms of the formation of oligomers and N-heterocycles were investigated. The chemical composition and the product distribution were also estimated and characterized by conventional transition state theory considering solvent cage and diffusion-limited effects (Methods). The aerosol growth rate for the heterogeneous chemistry of GL was also evaluated under different atmospheric conditions. We also paid a special attention on the key factors in the formation of SOA and BrC from GL to provide insight into the important role of the aqueous-phase chemistry of GL.

2 Methods

All quantum chemical calculations were performed be means of Gaussian 09 program (Frisch et al., 2009). The solvent effect of water in the aqueous phase was considered by a continuum solvation model (SMD) (Marenich et al., 2009). The solvation free energy includes two components: the bulk electrostatic contribution and the cavity-dispersion-solvent-structure contribution arising from short-range interactions between the solute and solvent molecules. Geometry optimization of all stationary points (SPs) such as reactants, transition states (TSs), intermediates, and products, was calculated using the M06-2X functional (Zhao and Truhlar, 2008) with the 6-311G(d,p) basis set (Ji et al., 2017; Ji et al., 2020), i.e., the M06-2X/6-311G(d,p) level, which has shown good performance in describing the geometrical optimization of the heterogeneous reactions of small α-dicarbonyls (Ji et al., 2020; Shi et al., 2020). Thermodynamic contributions and harmonic vibrational frequencies were calculated at the same level as that for geometry optimization to identify all SPs as either a TS (exactly with only one imaginary frequency) or the minima (zero imaginary frequency). Intrinsic reaction coordinate (IRC) calculations were implemented to construct the minimum energy pathway (MEP), verifying that each TS accurately connected the corresponding reactants and products. At the same level, TS was searched by examining the SP using the TS keyword in geometry optimization, while the absence of a TS was confirmed if no energy exceeded the bond dissociation energy along the reaction coordinate (Ji et al., 2020). The TSs for four deprotonation pathways in GL+MA/AM reaction systems were identified at the M06-2X/6-311G(d) level because none of them were searched at the M06-2X/6-311G(d,p) level (detailed discussion in Supporting Information). The pointwise potential curve (PPC) scanning was performed to further confirm a barrierless process at the M06-2X/6-311G(d,p) level (Hazra and Sinha, 2011). For this method, all other geometric parameters were fully optimized, except for fixing the internal breaking or forming bond length (detailed in Supporting Information).

Based on the optimized structures mentioned above, single-point energy (SPE) calculation was performed to refine potential energy surface (PES) with a more flexible basis set 6-311+G(3df,3pd), i.e., at the M06-2X/6-311+G(3df,3pd) level.

For simplicity, hereinafter they were denoted as the X//Y, i.e., M06-2X//M06-2X level, where Y is a SPE calculation at the M06-2X/6-311+G(3df,3pd) level and X is the geometry optimized at the M06-2X/6-311G(d,p) level. To further evaluate the results at the M06-2X//M06-2X level, a higher-level calculation using the CCSD(T) method with the flexible 6-311+G(2df,2p) basis set was performed to refine the PESs. The CCSD(T) method (Lutnaes et al., 2009; Raghavachari and Trucks, 1989), i.e., coupled cluster approach with single and double substitutions including a perturbative estimation of connected triples substitutions, corresponds to a higher electronic correlation method. As discussed in Supporting Information (SI), the M06-2X//M06-2X level is suitable to predict energies and kinetics, and also represents a compromise between computational efficiency and accuracy.

The rate constants (k) of the pathways with TSs were calculated using the conventional transition state theory (TST) (Gao et al., 2014; Galano and Alvarez-Idaboy, 2009) based on the above PES information:

$$k = \sigma \frac{k_B T}{h} \exp(\frac{-\Delta G^{\ddagger}}{RT}) , \tag{1}$$

where h and k_B are the Planck and Boltzmann constants, respectively, $\Delta G^{\ddagger}$ represents the activation barrier energy with the thermodynamic contribution corrections and solvent cage effects, and σ is the reaction path degeneracy. To simulate realistic conditions in the solution, the rate constants are refined by using solvent cage effects (Okuno, 1997) and diffusion-limited effects (Collins and Kimball, 1949). For some of the reactions with low free energy barriers, the rate constants are found to close to the diffusion-limit, which is calculated using the Collins-Kimball theory (Gao et al., 2014). The k values of the pathways without TSs are controlled by the diffusion-limit effect and thereby equal to the diffusion-limited rate constants:

$$k_D = 4\pi R D_{AB} N_A , \tag{2}$$

where R is the reaction distance, N_A denotes the Avogadro number, and D_{AB} represents the mutual diffusion coefficient of reactants. The branching ratio (Γ) was determined by the following equation:

$$\Gamma = \frac{k}{k_{total}} , \tag{3}$$

where the k corresponds to the rate constant of each pathway, and the k_{total} is the sum of the k value for each parallel pathway. The detailed description of kinetics was displayed in SI.

3 Results and discussion

3.1 Ion-mediated initial reaction of GL

The ion-mediated initial reactions of GL proceed via either proton-mediated ($R_{H+}1$) or hydroxyl ion (OH^-)-mediated ($R_{OH-}1$) hydration (Figs. 1a and S1a), yielding cationic (CIs) or anionic intermediates (AIs). As discussed in SI, no TS is identified by PPC scanning for all pathways in ion-mediated reactions (Fig. S2a). That is, all ion-mediated pathways are barrierless processes unless otherwise stated. Fig. 2 presents the natural population analysis of key species using natural bond orbital

(NBO) method (Glendening et al., 2011), and Fig. S3 lists the optimized geometries of all SPs. From a geometrical point of view, GL belongs to the C_{2h} point group, and the positions of two carbonyl groups are equivalent. The two carbonyl O-atoms and C-atoms exhibit the most negative and positive natural charges of -0.532 e and 0.383 e, respectively, indicating that the proton- and OH$^-$-mediated reactions of GL start from carbonyl groups.

The PESs of possible pathways in the ion-mediated reaction of GL are presented in Figs. 1a and S1. For proton-mediated pathways ($R_{H+}1$), protonation of carbonyl O-atom ($R_{H+}11$) is largely exothermic with a reaction energy (ΔG_r) of -96.9 kcal mo1^{-1}, to form the CI11. Alternatively, protonation of GL can be also initiated by the hydronium ion (H_3O^+) with a barrierless process. As shown in Fig. S1, water protonation can provide the corresponding ΔG_r value of -111.0 kcal mol^{-1}, and thus for the convenience of discussion, the following proton-mediated pathways refer specially to the hydrogen ions (H^+) initiated reactions. The nucleophilic attack of GL by OH$^-$ ($R_{OH-}11$) is also exothermic with the ΔG_r value of -13.4 kcal mo1^{-1}, to yield the AI11. The small exothermicity of $R_{OH-}11$ implies thermodynamically unfavorable formation of AI11. Table S1 lists the k values of $R_{H+}11$ and $R_{OH-}11$ pathways as well as the k_{total} of R1. Herein, the k_{total} value of the ion-initiated reactions (the sum of the k values of $R_{H+}11$ and $R_{OH-}11$ pathways) is 6.02×10^9 M^{-1} s^{-1}, and the k of the $R_{OH-}11$ pathway contributes 30% to the k_{total}. Further, considering the moderately acidic condition inside fine particles (Liu et al., 2017; Guo et al., 2012), proton-mediated reaction of GL is of major significance in the troposphere, and thus, the subsequent reactions of CIs are mainly considered in the following part.

As shown in Fig. S3, the length of the C−O bond in CI11 is elongated to 1.24 Å, facilitating the subsequent hydration reaction ($R_{H+}12$). CI11 reacts via hydration and dehydration to yield diol (DL) with successive increasing in ΔG_r values ranging from -8.0 to -1.0 kcal mol^{-1}. Subsequently, DL protonation occurs at the carbonyl ($R_{H+}21-1$) or hydroxyl ($R_{H+}22-1$) O-atom, leading to the formation of tetrol (TL) and the first-generation carbenium ion (1st-CB1) (Figs. 1a and S1b). The $R_{H+}21-1$ and $R_{H+}22-1$ pathways to form CI21-1 and CI22-1 are also strongly exothermic with the ΔG_r values of -103.0 and -104.4 kcal mol^{-1}, respectively. The pathway for CI21-1 to TL processes via hydration and deprotonation with successive increasing in ΔG_r values, and CI22-1 to 1st-CB1 reaction via deprotonation corresponds to a slightly increasing ΔG_r value, suggesting that both TL and 1st-CB1 are the dominant intermediates.

As shown in Table S1, the k values of $R_{H+}21-1$ and $R_{H+}22-1$ pathways are all 4.14×10^9 M^{-1} s^{-1} and their half-lives ($t_{1/2}$) are lower than ~10^{-4} s. The $t_{1/2}$ was calculated using the formula, $t_{1/2}=1/(k \times [H^+])$, where k is the rate constant of the $R_{H+}21-1$ or $R_{H+}22-1$ pathway and [H^+] is the concentration of the hydrogen ion (10^{-6} M) in the weakly acidic solution. It implies the rapid conversion from DL to TL and 1st-CB1, in line with the experimental results that the abundance of GL monohydrate is lower than 2% in acidic conditions (Malik and Joens, 2000). As discussed in SI, it further confirms that the direct hydration ($R_{H2O}1$ and $R_{H2O}2$) and OH$^-$-mediated hydration ($R_{OH-}1$ and $R_{OH-}2$) are kinetically and thermodynamically hindered. Hence, the cation-mediated initial reaction of GL, as the dominant route in the aqueous phase, is mainly focused on and explored in the following study.

3.2 Oligomerization mechanisms without methylamine/ammonia

3.2.1 Dimerization

The dominant intermediates, TL and 1st-CB1, can subsequently conduct electrostatic attraction with each other. As shown in Fig. S3, the C–O(H) bond of 1st-CB1 after protonation is elongated by 0.05 Å relative to the C=O bond of GL, attributable to the presence of a carbenium ion center. The natural charge of the carbenium ion center in 1st-CB1 is 0.547 e (Fig. 2), implying that it is liable to nucleophilic addition with negative natural charge center of TL via electrostatic attraction. All possible pathways involved in nucleophilic addition between 1st-CB1 and TL are constructed and depicted in Figs. 1b and S4a.

The nucleophilic addition of 1st-CB1 with TL ($R_{TL}41$) is an exothermic process with the ΔG_r value of -6.7 kcal mol^{-1}. The subsequent hydration ($R_{TL}42$) and deprotonation ($R_{TL}43$) exhibit a small ΔG_r value of -5.2 kcal mol^{-1}, to yield a ring-opening dimer (ROD1) that has been identified under acidic condition using thermal desorption-ion drift-chemical ionization mass spectrometry (TD-ID-CIMS) (Li et al., 2021b). On the other hand, 1st-CB2 is produced via protonation ($R_{H+}31$) and dehydration ($R_{H+}32$) of TL, similar to the formation of 1st-CB1 (Fig. S1c). 1st-CB2 is also attacked by TL ($R_{TL}51$) to form $CI_{TL}51$, which then proceed via hydration ($R_{TL}52$) and deprotonation ($R_{TL}53$) to yield ROD3 (Fig. S4b). An intermolecular isomerization pathway exists from ROD1 to ROD3 (R6, Fig. S4c). That is, ROD3 can be formed from ROD1 via protonation ($R_{H+}61$), hydration ($R_{H+}62$ and $R_{H+}63$), and deprotonation ($R_{H+}64$), with the total ΔG_r value of -113.5 kcal mol^{-1}. As shown in Fig. 2, the natural charge of C-atom in 1st-CB2 is more positive than that in 1st-CB1, implying a stronger electrostatic attraction between 1st-CB2 and TL. However, the ΔG_r value of $R_{TL}51$ is -3.1 kcal mol^{-1}, which is higher than that of $R_{TL}41$ (Fig. S4a-b). It indicates that the reactivity of the positive charge centers in carbenium ions is affected by both electrostatic attraction and steric effect.

The nucleophilic addition reaction of 1st-CBs with DL is also illuminated and presented in Figs. 1b and S4a-b, although DL is not the most dominant products in the aqueous-phase reaction of GL. Both ROD2 and ROD1 are generated from DL, respectively, through the analogous pathways to $R_{TL}4$ and $R_{TL}5$. As shown in Fig. 2, the hydroxyl O-atom in TL has a larger negative natural charge than that in DL, implying that there is a stronger electrostatic attraction between 1st-CBs and TL. In addition, the ΔG_r values of association reactions of 1st-CBs with DL are -5.3 (for 1st-CB1) and -1.8 (for 1st-CB2) kcal mol^{-1}, respectively, which are less negative than those with TL. It indicates that the most abundant dimers correspond to the oligomeric pathways arising from 1st-CBs with TL in weakly acidic condition.

3.2.2 Trimerization and oligomerization

Similar to the formation of 1st-CBs, as shown in Fig. 1b, the ring-opening dimers then repeat protonation and dehydration to form six second-generation carbenium ions (2nd-CBs) (Fig. S5), which further engage in the formation of cyclic dimers (CDs) or ring-opening trimers (ROTs). Figs. S6-S7 present the schematic energy diagram for the formation of CDs and ROTs, and Fig. S8 depicts the optimized geometries of SPs involved in the pathways mentioned above. Totally, three CDs and nine

ROTs are produced and identified via R8-R20 routes and the overall schematic diagram is shown in Fig. 1b. For example, protonation (R_{H+}81-1) and dehydration (R_{H+}81-2) of ROD1 yield 2nd-CB1, which undergoes intramolecular isomerization pathway to produce CI111 (R111). CI111 is further hydrolyzed (R112) and deprotonated (R113) to yield CD1. Alternatively, 2nd-CB1 association with TL and DL yields CI_{TL}151 and CI_{DL}151, respectively, and their subsequent pathways are similar to the pathways of the formation of RODs, resulting in the formation of ROT1 and ROT2 (Fig. S7a). Current results reveal that cyclic oligomers are difficult to be formed from the CBs with the positive charge center close to O(H) atom, such as 2nd-CB2 and 2nd-CB4 in Fig. 1b. Also, the isomeric conversion can also occur among the nine ROTs via protonation, hydration, and deprotonation processes (R21-R27 in Fig. S9).

Similar to dimerization pathways, the nine ROTs further engage in protonation and dehydration reactions to produce twenty-five third-generation carbenium ions (3rd-CBs) (R28-R36 in Fig. 3). In this study, the configurations of oligomers with the lowest energies are applied because many isomers of dimers and trimers can be yielded. Subsequently, twenty-five 3rd-CBs undergo intramolecular isomerization, hydration, and deprotonation to further yield twelve cyclic trimers (CTs) (Fig. S10 and Table S2). Based on kinetic rate calculations, the k values of dimer and trimer formation are ~10^9 M^{-1} s^{-1} in the aqueous phase, limited by liquid-phase diffusion. It should be pointed out that the rate constants of dimer and trimer formation obtained from our theoretical calculations are distinct from those previously investigated by Ervens and Volkamer (Ervens and Volkamer, 2010). The rate constants in this previous study are obtained to be ~10^{-2} and ~100 M^{-1} s^{-1} for dimer and trimer formation based on the direct nucleophilic addition between GL and GL or GL and GL hydrates. Our protonation-initiated cationic oligomerization involves nucleophilic addition of diol/tetrol to carbenium ions, which is fast and barrierless. Hence, the formation of various ring-opening/cyclic dimers and trimers is initiated by protonation and subsequently propagated via the electrostatic attraction, with the rate constants of ~10^9 M^{-1} s^{-1}, ultimately contributing to SOA formation.

3.3 Oligomerization mechanisms with methylamine/ammonia

As shown in Fig. 2, a strong electrostatic attraction exists between 1st-CBs and AM or MA because N-atoms exhibit large negative natural charges (-0.875 e for MA and -1.078 e for AM). Hence, the carbenium ion-mediated oligomerization of GL with MA/AM to form N-oligomers is simulated and presented in Fig. 4. Figs. S11-S12 depict the optimized geometries of key SPs. Also, the involved cation-mediated pathways default to barrierless processes unless stated (Fig. S2b).

3.3.1 The nucleophilic addition of 1st-CBs with MA

Attack of 1st-CBs by MA results in four N-containing ring-opening dimer (N-ROD) formation. For example, such multistep processes of 1st-CB1 with MA are shown as the following (Fig. 4a-b),

$$R_{MA}60\text{-}R_{MA}61:\ 1^{st}\text{-CB1} \xrightarrow{\mathbf{R_{MA}601:}\ +\ MA} CI_{MA}601 \xrightarrow{\mathbf{R_{MA}602:}\ +\ SO_4^{2-}} TS_{MA}601 \xrightarrow{-\ HSO_4^-} \text{N-ROD}_{MA}1 \xrightarrow{\mathbf{R_{MA}611:}\ +\ H^+} CI_{MA}611 \xrightarrow{\mathbf{R_{MA}612:}\ -H_2O}$$

$$CI_{MA}612 \xrightarrow{\mathbf{R_{MA}613:}\ +\ SO_4^{2-}} TS_{MA}611 \xrightarrow{-\ HSO_4^-} \text{N-ROD}_{MA}2$$
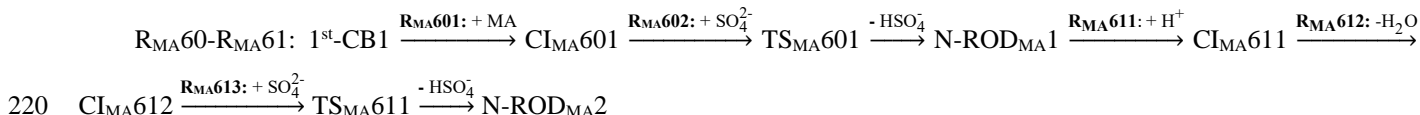
For the association pathway of 1st-CB1 with MA ($R_{MA}601$), the ΔG_r value is -43.2 kcal mol^{-1}. In CI$_{MA}601$, the length of the formed C−N bond is 1.50 Å (Fig. S12a). Unlike the oligomerization without MA, the subsequent deprotonation of CI$_{MA}601$ is difficult to be initiated by H_2O (Fig. S13, as discussed in SI). It implies that deprotonation from N-containing CIs needs to be initiated by species with larger electronegativity than H_2O. Taking into account the real atmospheric conditions, in this study, deprotonation of the amino group in CI$_{MA}601$ is initiated by SO_4^{2-} ($R_{MA}602$). As shown in Fig. S14, the natural charge center of CI$_{MA}601$ is located at the amino H-atom, which is readily abstracted by SO_4^{2-} to form N-ROD$_{MA}1$. The $R_{MA}602$ pathway proceeds via a TS with the small activation energy ($\Delta G^{\ddagger}$) of -1.7 kcal mol^{-1}. A pre-reactive complex (COM$_{MA}601$) is identified prior to the TS and the corresponding ΔG_r value is -1.0 kcal mol^{-1}, which is lower than that of the corresponding reactants. As illustrated in SI, the structure of COM$_{MA}601$ is similar to those of the reactants, except for the broken bonds. As shown in Fig. 4b, protonation of N-ROD$_{MA}1$ at the hydroxyl group ($R_{MA}611$) yields CI$_{MA}611$ with the ΔG_r value of -122.8 kcal mol^{-1}. The subsequent dehydration of CI$_{MA}611$ ($R_{MA}612$) possesses the small exothermicity with the G_r value of -5.7 kcal mol^{-1}, to form CI$_{MA}612$. Similar to the subsequent reaction of CI$_{MA}601$, deprotonation of CI$_{MA}612$ is also initiated by SO_4^{2-} ($R_{MA}613$), to form the other N-ROD (N-ROD$_{MA}2$), with the $\Delta G^{\ddagger}$ value of -7.3 kcal mol^{-1}. In addition, there also exist an intermolecular isomerization pathway from N-ROD$_{MA}2$ to N-ROD$_{MA}3$ via protonation, hydration, and deprotonation (Fig. 4c),

$$R_{MA}62: \text{N-ROD}_{MA}2 \xrightarrow{R_{MA}621:\, +\,H^+} \text{CI}_{MA}621 \xrightarrow{R_{MA}622:\, +\,H_2O} \text{CI}_{MA}622 \xrightarrow{R_{MA}623:\, +\,H_2O} \text{CI}_{MA}623 \xrightarrow{R_{MA}624:\, -\,H_3O^+} \text{N-ROD}_{MA}3$$
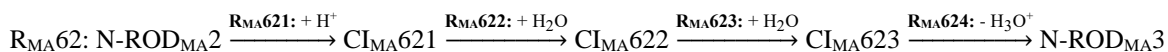
For the $R_{MA}62$ pathway, the total ΔG_r value for protonation, hydration, and deprotonation of N-ROD$_{MA}2$ is -108.1 kcal mol^{-1}, yielding N-ROD$_{MA}3$. N-ROD$_{MA}3$ then repeats protonation and dehydration to yield N-containing CBs (N-1st-CBs), which subsequently engage in the nucleophilic addition with MA to in sequence form N-containing ring-opening trimers, N-ROT$_{MA}1$ and N-ROT$_{MA}2$, (Fig. 4c-e),

$$R_{MA}63\text{-}R_{MA}65: \text{N-ROD}_{MA}3 \xrightarrow{R_{MA}631:\, +\,H^+} \text{CI}_{MA}631 \xrightarrow{R_{MA}632:\, -\,H_2O} \text{N-}1^{st}\text{-CB}_{MA}1 \xrightarrow{R_{MA}641:\, +\,MA} \text{CI}_{MA}641 \xrightarrow{R_{MA}642:\, +\,SO_4^{2-}} \text{TS}_{MA}641$$
$$\xrightarrow{-\,HSO_4^-} \text{N-ROT}_{MA}1 \xrightarrow{R_{MA}651:\, +\,H^+} \text{CI}_{MA}651 \xrightarrow{R_{MA}652:\, -\,H_2O} \text{CI}_{MA}652 \xrightarrow{R_{MA}653:\, +\,SO_4^{2-}} \text{TS}_{MA}651 \xrightarrow{-\,HSO_4^-} \text{N-ROT}_{MA}2$$
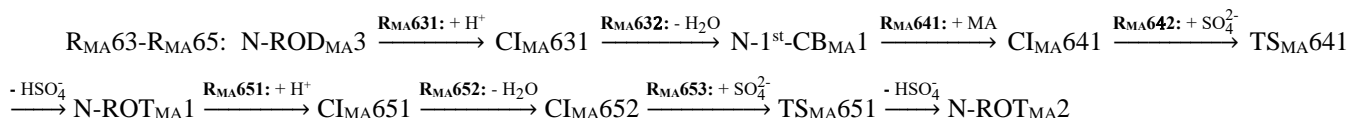
Subsequently, N-ROT$_{MA}2$ undergoes the nucleophilic addition with 1st-CBs rather than protonation, attributing to geometric characteristics, i.e., no hydroxyl groups in N-ROT$_{MA}2$ to protonation (Fig. S11). For example, the reaction of N-ROT$_{MA}2$ with 1st-CB1 to form N-heterocycles involve the following stepwise pathways (Fig. S15),

$$R_{MA}66\text{-}R_{MA}67: \text{N-ROT}_{MA}2 \xrightarrow{R_{MA}661:\, +\,1^{st}\text{-CB1}} \text{CI}_{MA}661 \xrightarrow{R_{MA}662:\, +\,TS_{anti \to syn}} \text{CI}_{MA}662 \xrightarrow{R_{MA}663:\, +\,SO_4^{2-}} \text{TS}_{MA}662 \xrightarrow{-\,HSO_4^-} \text{N-IM}_{MA}1$$
$$\xrightarrow{R_{MA}671:\, +\,H^+} \text{CI}_{MA}671 \xrightarrow{R_{MA}672:\, -\,H_2O} \text{TS}_{MA}671 \to \text{N-CT}_{MA}1$$
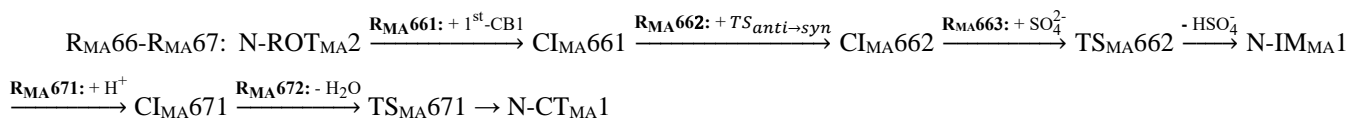
The nucleophilic addition of N-ROT$_{MA}2$ with 1st-CB1 ($R_{MA}66$) is largely exothermic with the ΔG_r value of -33.8 kcal mol^{-1} to overcome the barrier of subsequent intramolecular torsion and H-abstraction pathways. The intramolecular torsion from CI$_{MA}661$ to CI$_{MA}662$ proceeds via a TS, with the small $\Delta G^{\ddagger}$ value of 5.1 kcal mol^{-1}. The $\Delta G^{\ddagger}$ value of the H-abstraction pathway ($R_{MA}663$) is 18.4 kcal mol^{-1}. Subsequently, protonation of N-IM$_{MA}1$ occurs at hydroxyl group to form CI$_{MA}671$, which undergoes dehydration via a TS, yielding N-containing cyclic tetramer (N-CT$_{MA}1$, in Fig. S15). The $\Delta G^{\ddagger}$ and ΔG_r

values of $R_{MA}672$ are 17.3 and -89.4 kcal mol^{-1}, respectively. The association reaction of 1st-CB2 with MA are also investigated and discussed in SI via the similar stepwise pathways of 1st-CB1 with MA (Figs. S16-S17), yielding a N-containing cyclic tetramer (N-CT$_{MA}$2). The intermolecular isomerization reaction from N-CT$_{MA}$1 to N-CT$_{MA}$2 is also observed (Fig. S18a). All N-containing dimers, trimers and tetramers subsequently contribute to N-heterocycles, which are the important precursors of BrC aerosols. Because all deprotonation reactions proceed via the corresponding TS in the presence of MA and their rate constants fall in the range of $(1.17-1.30) \times 10^9$ M^{-1} s^{-1} (Table S3), deprotonation is the rate-limiting step to propagate N-heterocycles. It implies that N-heterocycle formation is more dependent on the content of inorganic compounds or inorganic salts in aerosol rather than particle acidity.

3.3.2 The nucleophilic addition of 1st-CBs with AM

The carbenium ion-mediated reactions to N-heterocycles in the presence of AM involves the stepwise processes (Figs. 4 and S15-S17), similar to the nucleophilic addition of 1st-CBs with MA. That is, the formation of N-heterocycles from GL with AM involves three vital steps (Fig. S19): (1) the nucleophilic reaction of AM with CBs to form N-RODs, (2) protonation and dehydration of N-RODs to yield N-containing CBs, and (3) the formation and propagation of N-heterocycles by the association reactions of N-containing CBs with AM. Alternatively, GL can be attacked by ammonium ion (NH$_4^+$) to produce CI$_{AM}$601 due to the equilibrium reaction between AM and NH$_4^+$ in solution, with the ΔG_r value of -0.9 kcal mol^{-1} (Fig. 4a). CI$_{AM}$601 engages in vital steps (2) and (3) to finally form N-heterocycles (N-CT$_{AM}$1 and N-CT$_{AM}$2). Different from the case in the presence of MA, N-CT$_{AM}$1 and N-CT$_{AM}$2 can subsequently proceed deprotonation to form N-CT$_{AM}$3 and N-CT$_{AM}$4 (Fig. S18b), respectively, because of the presence of H-atoms in amino groups of N-CT$_{AM}$1 and N-CT$_{AM}$2 and absence in N-CT$_{MA}$1 and N-CT$_{MA}$2. This explains that N-CT$_{AM}$3 and N-CT$_{AM}$4 are identified in the presence of ammonium salts [such as (NH$_4$)$_2$SO$_4$] (Lee et al., 2013; Yu et al., 2011), while N-CT$_{MA}$1 is observed in the presence of MA (De Haan et al., 2009). Hence, the carbenium ion-mediated mechanism also provides a key pathway for the formation of BrC from GL in the presence of ammonium salts.

3.4 Estimation of the heterogeneous GL reaction rates and growth rates of SOA and BrC formation

To evaluate the atmospheric regions where the heterogeneous reaction of GL will have significance, the heterogeneous GL reaction rates and the growth rates of SOA and BrC formation (GR_{SOA} and GR_{BrC}) are estimated under rural, remote, and urban conditions using the predicted carbenium ion-mediated reaction mechanism of GL mentioned above. First, the heterogeneous GL reaction rates without or with MA/AM were driven by the expression as follows,

$$k_{rate} = k \times C_g \times \gamma_{GL} , \tag{4}$$

where C_g is the gas phase concentration under rural, remote and urban conditions, k is the calculated rate constant of protonation reaction (4.20×10^9 M^{-1} s^{-1}) in the absence of MA/AM or deprotonation ($1.17/1.32 \times 10^9$ M^{-1} s^{-1}) in the presence of MA/AM, and γ_{GL} is uptake coefficient of GL under urban condition.

The heterogeneous GL reaction rate [k_{rate}(total)] is the sum of the rates without and with MA/AM. Table 1 lists the k_{rate}

285   without and with MA/AM and k_{rate}(total) under rural, remote, and urban conditions as well as the available experimental data (Liggio et al., 2005a). The k_{rate}(total) values are 4.62×10^{-3}, 9.25×10^{-4}, and 1.85×10^{-3} s^{-1} under above mentioned three conditions. The k_{rate} value under urban condition almost agrees with that of the experimental data and is slightly larger than those of the experimental data under other conditions (Liggio et al., 2005a). The lower values under remote and rural conditions are explained by the γ_{GL} used here, which is more suitable for the urban condition (Liggio et al., 2005a). Second,

290   the growth rate (GR_{SOA}) (Ji et al., 2020) is expressed as:

$$GR_{SOA} = \frac{d[GL_{proton}]}{dt} \times \text{AWC} , \qquad (5)$$

where $\frac{d[GL_{proton}]}{dt}$ represents the rate of GL protonation given by $k_{rate} \times [\text{H}^+] \times H_{GL}$, where k_{rate} is the rate of heterogeneous GL reaction without MA/AM (in Table 1), and [H$^+$] is the concentration of the hydrogen ion (10^{-6} M) in the weakly acidic solution, and AWC is the aerosol water content (1.1×10^{-10}) (Ji et al., 2020). The GR_{BrC} is also calculated using the formula

295   (5), where $\frac{d[GL_{proton}]}{dt}$ is replaced by $\frac{d[GL_{deproton}]}{dt} = k_{rate} \times [\text{SO}_4^{2-}] \times H_{GL}$, i.e.,

$$GR_{BrC} = k_{rate} \times [\text{SO}_4^{2-}] \times H_{GL} \times \text{AWC} , \qquad (6)$$

where k_{rate} is the rate of heterogeneous GL reaction with MA/AM, and [SO$_4^{2-}$] is the concentration of SO$_4^{2-}$ (5.0×10^{-7} M) in the weakly acidic solution. Considering that the deprotonation occurs readily by acidic anions (eg., SO$_4^{2-}$), the obtained GR_{BrC} values in this study may be underestimated. The GR_{SOA} and GR_{BrC} values under the different atmospheric conditions

300   are also presented in Table 1. The GR_{SOA} is 1.41 µg m^{-3} h^{-1} under urban condition, which is larger than the GR_{BrC} (0.44 µg m^{-3} h^{-1} for MA and 0.45 µg m^{-3} h^{-1} for AM). The total growth rate (the sum of the GR_{SOA} and GR_{BrC} values) is also consistent with the experimental data (1.44 µg m^{-3} h^{-1}) (Liggio et al., 2005a). Hence, it is reasonable to expect the occurrence of carbenium ion-mediated mechanism in ambient aerosols as a means of SOA and BrC formation.

4 Conclusions

305   This study provides a valuable insight into the aqueous chemistry of GL and also reveals the rate-limiting steps in the absence and presence of amines/ammonia. In the absence of amines/ammonia (Fig. 5), the cation-mediated oligomerization is characterized by barrierless pathways and strong electrostatic attraction as follows: (I) protonation, hydration, and deprotonation of GL to yield DL and TL, (II) protonation and dehydration to yield CBs, and (III) the formation of dimers from the association reactions of CBs with DL and TL. Each dimer repeats steps (II) and (III) to propagate the

310   oligomerization. In the presence of amines/ammonia, the step (III) starts from nucleophilic addition of CBs with amines/ammonia rather than with DL/TL due to the stronger electrostatic attraction between CBs and amines/ammonia (Fig. 2). However, the key mechanistic step in the propagation of N-heterocycles is deprotonation of N-containing cationic

intermediates. Our results of two distinct mechanisms indicate that BrC formation is more dependent on the aerosol content of inorganic compounds or inorganic salts rather than particle acidity, compared with the formation of SOA.

315   On the other hand, there exist the competing pathways with the initial protonation pathway for the cationic oligomerization of GL without and with amines/ammonia, (i.e., the association reactions of CIs with OH$^-$). These competing pathways lead to CIs returning back the corresponding reactants and affect the fate of GL. Fig. S20 and Table S1 present the ΔG_r and k values of the association reactions for some key CIs with OH$^-$. Generally, the fate of CIs at each step is dominantly determined by the initial protonation rather than the reaction with OH$^-$. For example, the ΔG_r value of the association

320   pathway of CI11 with OH$^-$ is -66.8 kcal mol^{-1}, and its k value is 1.47×10^9 M^{-1} s^{-1}. Compared with the protonation of GL to CI11, this reaction is thermodynamically and kinetically unfavorable. The branching ratios show that 70% of GL proceeds protonation pathway to finally form DL. Because protonation is favorable in the acidic aerosol, the cation-mediated oligomerization of GL without and with amines/ammonia can efficiently proceed to contribute to SOA and BrC under the atmospheric conditions.

325   Using our predicted heterogeneous GL reaction rates, the aqueous heterogeneous lifetime (τ) of GL is estimated to be 3.60 min under urban condition, somewhat smaller than that of experimental data (5.0 min) (Liggio et al., 2005a). However, the τ values are 89 and 61 min under rural and remote conditions due to low GL level, respectively (Liggio et al., 2005a). It indicates a more important role of aqueous heterogenous reaction of GL in urban air quality relative to other conditions. On the other hand, the τ values determined here for rural, remote, and urban conditions are all lower than those of the photolysis

330   (211 min) and photooxidation of GL (Liggio et al., 2005a). Especially, the τ value under urban condition is significantly shorter than the total gas-phase loss (125 min) (Liggio et al., 2005a). The results indicate that even under relatively clean conditions, the heterogeneous GL loss rates are faster than the loss rates due to other gas phase processes and are much significantly rapid in polluted regions. Given that GL contributes to 6.9% of the total radical production at midday (Aiello, 2003), the heterogeneous GL loss to particle implies the reduction of HO$_x$ and demands further study. Our work reveals the

335   fundamental chemical mechanism of SOA and BrC formation from small α-dicarbonyls and also provides the kinetic and mechanistic data for atmospheric modeling to assess the budget of SOA and BrC formation on urban, regional, and global scales.

Data availability. All raw data can be provided by the corresponding authors upon request.

Supplement. The supplement related to this article is available on the EGU Publications website.

340 **Author contributions.** JYM and SQJ designed research; JYM, SQJ, MXH, GL, WJX and LYX performed research; JYM, SQJ, MXH, GL, WJX, LYX, GYP, LGY, ZRY and ATC analyzed data; JYM and SQJ wrote the paper. JYM, MXH, ZRY and ATC reviewed and edited the paper.

Competing interests. The contact author has declared that neither they nor their co-authors have any competing interests.

Disclaimer. Publisher's note: Copernicus Publications remains neutral with regard to jurisdictional claims in published maps
345 and institutional affiliations.

Financial support. This work was financially supported by National Natural Science Foundation of China (grant nos. 42077189 and 4201001008), Natural Science Foundation of Guangdong Province, China (grant nos. 2019B151502064), Local Innovative and Research Teams Project of Guangdong Pearl River Talents Program (grant nos. 2017BT01Z032), and Science and Technology Key Project of Guangdong Province, China (grant nos. 2019B110206002).

350 **References**

Acosta Navarro, J. C., Smolander, S., Struthers, H., Zorita, E., Ekman, A. M., Kaplan, J. O., Guenther, A., Arneth, A., and Riipinen, I.: Global emissions of terpenoid VOCs from terrestrial vegetation in the last millennium, J. Geophys. Res. Atmos., 119, 6867-6885, https://doi.org/10.1002/2013JD021238, 2014.

Aiello, M.: An automated instrument for the quantitation of atmospheric carbonyls: measurements and interpretation in
355 southern ontario, Ph.D. thesis, York Univ., Toronto, Ont., Canada, 256 pp., 2003.

Altieri, K. E., Carlton, A. G., Lim, H. J., Turpin, B. J., and Seitzinger, S. P.: Evidence for oligomer formation in clouds: reactions of isoprene oxidation products, Environ. Sci. Technol., 40, 4956-4960, https://doi.org/10.1021/es052170n, 2006.

Avzianova, E. and Brooks, S. D.: Raman spectroscopy of glyoxal oligomers in aqueous solutions, Spectrochim. Acta., A,
360 101, 40-48, https://doi.org/10.1016/j.saa.2012.09.050, 2013.

Cerqueira, M. A., Pio, C. A., Gomes, P. A., Matos, J. S., and Nunes, T. V.: Volatile organic compounds in rural atmospheres of central Portugal, Science of The Total Environment, 313, 49-60, https://doi.org/10.1016/s0048-9697(03)00250-x, 2003.

Collins, F. C. and Kimball, G. E.: Diffusion-controlled reaction rates, J. Colloid Sci., 4, 425-437,
365 https://doi.org/10.1016/0095-8522(49)90023-9, 1949.

De Haan, D. O., Tolbert, M. A., and Jimenez, J. L.: Atmospheric condensed-phase reactions of glyoxal with methylamine, Geophysical Research Letters, 36, L11819, https://doi.org/10.1029/2009gl037441, 2009.

De Haan, D. O., Hawkins, L. N., Jansen, K., Welsh, H. G., Pednekar, R., de Loera, A., Jimenez, N. G., Tolbert, M. A., Cazaunau, M., Gratien, A., Bergé, A., Pangui, E., Formenti, P., and Doussin, J. F.: Glyoxal's impact on dry ammonium salts: fast and reversible surface aerosol browning, Atmos. Chem. Phys., 20, 9581-9590, https://doi.org/10.5194/acp-20-9581-2020, 2020.

Ervens, B. and Volkamer, R.: Glyoxal processing by aerosol multiphase chemistry: towards a kinetic modeling framework of secondary organic aerosol formation in aqueous particles, Atmos. Chem. Phys., 10, 8219-8244, https://doi.org/10.5194/acp-10-8219-2010, 2010.

Frisch, M. J., Trucks, G.W., Schlegel, H. B., Scuseria, G. E., Robb,, M. A., C., J. R., Scalmani, G., Barone, V., Petersson, G., A., N., H., Li, X., Caricato, M., Marenich, A. V., Bloino,, J., J., B. G., Gomperts, R., Mennucci, B., Hratchian, H., P., O., J. V., Izmaylov, A. F., Sonnenberg, J. L., Williams,, Ding, F., Lipparini, F., Egidi, F., Goings, J., Peng, B., Petrone,, A., H., T., Ranasinghe, D., Zakrzewski, V. G., Gao, J.,, Rega, N., Zheng, G., Liang, W., Hada, M., Ehara, M., Toyota,, K., F., R., Hasegawa, J., Ishida, M., Nakajima, T., Honda,, Y., K., O., Nakai, H., Vreven, T., Throssell, K., Montgomery, Jr., J. A., Peralta, J. E., Ogliaro, F., Bearpark, M. J., Heyd, J. J.,, Brothers, E. N., Kudin, K. N., Staroverov, V. N., Keith, T. A.,, Kobayashi, R., Normand, J., Raghavachari, K., Rendell, A. P.,, Burant, J. C., Iyengar, S. S., Tomasi, J., Cossi, M., Millam, J., M., K., M., Adamo, C., Cammi, R., Ochterski, J. W., Martin,, and R. L., M., K., Farkas, Ö., Foresman, J. B., and Fox, D. J: Gaussian09, Revision D.01, Gaussian, Inc., Wallingford CT., 2009.

Fu, T. M., Jacob, D. J., Wittrock, F., Burrows, J. P., Vrekoussis, M., and Henze, D. K.: Global budgets of atmospheric glyoxal and methylglyoxal, and implications for formation of secondary organic aerosols, J. Geophys. Res., 113, D15303, https://doi.org/10.1029/2007jd009505, 2008.

Galano, A. and Alvarez-Idaboy, J. R.: "Guanosine + OH radical reaction in aqueous solution: A reinterpretation of the UV-vis data based on thermodynamic and kinetic calculations", Org. Lett., 11, 5114-5117, https://doi.org/10.1021/ol901862h, 2009.

Galloway, M. M., Chhabra, P. S., Chan, A. W. H., Surratt, J. D., Flagan, R. C., Seinfeld, J. H., and Keutsch, F. N.: Glyoxal uptake on ammonium sulphate seed aerosol: Reaction products and reversibility of uptake under dark and irradiated conditions, Atmos. Chem. Phys., 9, 3331-3345, https://doi.org/10.5194/acp-9-3331-2009, 2009.

Gao, Y., Ji, Y., Li, G., and An, T.: Mechanism, kinetics and toxicity assessment of OH-initiated transformation of triclosan in aquatic environments, Water Res, 49, 360-370, https://doi.org/10.1016/j.watres.2013.10.027, 2014.

Ge, M., Tong, S., Wang, W., Zhang, W., Chen, M., Peng, C., Li, J., Zhou, L., Chen, Y., and Liu, M.: Important oxidants and their impact on the environmental effects of aerosols, J. Phys. Chem. A, 125, 3813-3825, https://doi.org/10.1021/acs.jpca.0c10236, 2021.

Glendening, E. D., Landis, C. R., and Weinhold, F.: Natural bond orbital methods, Wires Comput. Mol. Sci., 2, 1-42, https://doi.org/10.1002/wcms.51, 2011.

400 Gomez Alvarez, E., Viidanoja, J., Munoz, A., Wirtz, K., and Hjorth, J.: Experimental confirmation of the dicarbonyl route in the photo-oxidation of toluene and benzene, Environ. Sci. Technol., 41, 8362-8369, https://doi.org/10.1021/es0713274, 2007.

Gomez, M. E., Lin, Y., Guo, S., and Zhang, R.: Heterogeneous chemistry of glyoxal on acidic solutions. An oligomerization pathway for secondary organic aerosol formation, J. Phys. Chem. A, 119, 4457-4463, https://doi.org/10.1021/jp509916r,
405 2015.

Guo, J., Wang, Y., Shen, X., Wang, Z., Lee, T., Wang, X., Li, P., Sun, M., Collett, J. L., Wang, W., and Wang, T.: Characterization of cloud water chemistry at Mount Tai, China: Seasonal variation, anthropogenic impact, and cloud processing, Atmos. Environ., 60, 467-476, https://doi.org/10.1016/j.atmosenv.2012.07.016, 2012.

Hastings, W. P., Koehler, C. A., Bailey, E. L., and De Haan, D. O.: Secondary organic aerosol formation by glyoxal
410 hydration and oligomer formation: humidity effects and equilibrium shifts during analysis, Environ. Sci. Technol., 39, 8728-8735, https://doi.org/10.1021/es050446l, 2005.

Hazra, M. K. and Sinha, A.: Formic acid catalyzed hydrolysis of SO_3 in the gas phase: a barrierless mechanism for sulfuric acid production of potential atmospheric importance, J. Am. Chem. Soc., 133, 17444-17453, https://doi.org/10.1021/ja207393v, 2011.

415 Huang, M. Q., Cai, S. Y., Liao, Y. M., Zhao, W. X., Hu, C. J., Wang, Z. Y., and Zhang, W. J.: Theoretical studies on mechanism and rate constant of gas phase hydrolysis of glyoxal catalyzed by sulfuric acid, Chinese J. Chem. Phys., 29, 335-343, https://doi.org/10.1063/1674-0068/29/cjcp1509193, 2016.

Jang, M., Czoschke, N. M., Lee, S., and Kamens, R. M.: Heterogeneous atmospheric aerosol production by acid-catalyzed particle-phase reactions, Science, 298, 814-817, https://doi.org/10.1126/science.1075798, 2002.

420 Ji, Y., Shi, Q., Li, Y., An, T., Zheng, J., Peng, J., Gao, Y., Chen, J., Li, G., Wang, Y., Zhang, F., Zhang, A. L., Zhao, J., Molina, M. J., and Zhang, R.: Carbenium ion-mediated oligomerization of methylglyoxal for secondary organic aerosol formation, Proc. Natl. Acad. Sci. U. S. A., 117, 13294-13299, https://doi.org/10.1073/pnas.1912235117, 2020.

Ji, Y., Zhao, J., Terazono, H., Misawa, K., Levitt, N. P., Li, Y., Lin, Y., Peng, J., Wang, Y., Duan, L., Pan, B., Zhang, F., Feng, X., An, T., Marrero-Ortiz, W., Secrest, J., Zhang, A. L., Shibuya, K., Molina, M. J., and Zhang, R.: Reassessing
425 the atmospheric oxidation mechanism of toluene, Proc. Natl. Acad. Sci. U. S. A., 114, 8169-8174, https://doi.org/10.1073/pnas.1715304114, 2017.

Kroll, J. H., Ng, N. L., Murphy, S. M., Varutbangkul, V., Flagan, R. C., and Seinfeld, J. H.: Chamber studies of secondary organic aerosol growth by reactive uptake of simple carbonyl compounds, J. Geophys. Res., 110, D23207, https://doi.org/10.1029/2005jd006004, 2005.

430 Kua, J., Hanley, S. W., and Haan, D. O. D.: Thermodynamics and kinetics of glyoxal dimer formation: A computational study, J. Phys. Chem. A 112, 66-72, https://doi.org/10.1021/jp076573g, 2008.

Kua, J., Krizner, H. E., and De Haan, D. O.: Thermodynamics and kinetics of imidazole formation from glyoxal, methylamine, and formaldehyde: a computational study, J. Phys. Chem. A, 115, 1667-1675, https://doi.org/10.1021/jp111527x, 2011.

435 Lawson, S. J., Selleck, P. W., Galbally, I. E., Keywood, M. D., Harvey, M. J., Lerot, C., Helmig, D., and Ristovski, Z.: Seasonal in situ observations of glyoxal and methylglyoxal over the temperate oceans of the Southern Hemisphere, Atmos. Chem. Phys., 15, 223-240, https://doi.org/10.5194/acp-15-223-2015, 2015.

Lee, A. K., Zhao, R., Li, R., Liggio, J., Li, S. M., and Abbatt, J. P.: Formation of light absorbing organo-nitrogen species from evaporation of droplets containing glyoxal and ammonium sulfate, Environ. Sci. Technol., 47, 12819-12826, 440 https://doi.org/10.1021/es402687w, 2013.

Li, J., Han, Z., Sun, Y., Li, J., and Liang, L.: Chemical formation pathways of secondary organic aerosols in the Beijing-Tianjin-Hebei region in wintertime, Atmos. Environ., 244, 117996, https://doi.org/10.1016/j.atmosenv.2020.117996, 2021a.

Li, L., Zhong, J., Yan, Y., Zhang, J., Xu, J., Francisco, J. S., and Zeng, X. C.: Unraveling nucleation pathway in methane 445 clathrate formation, Proc. Natl. Acad. Sci. U. S. A., 117, 24701-24708, https://doi.org/10.1073/pnas.2011755117, 2020.

Li, Y., Ji, Y., Zhao, J., Wang, Y., Shi, Q., Peng, J., Wang, Y., Wang, C., Zhang, F., Wang, Y., Seinfeld, J. H., and Zhang, R.: Unexpected oligomerization of small alpha-dicarbonyls for secondary organic aerosol and brown carbon formation, Environ. Sci. Technol., 55, 4430-4439, https://doi.org/10.1021/acs.est.0c08066, 2021b.

Lian, X., Zhang, G., Yang, Y., Lin, Q., Fu, Y., Jiang, F., Peng, L., Hu, X., Chen, D., Wang, X., Peng, P. a., Sheng, G., and Bi, 450 X.: Evidence for the formation of imidazole from carbonyls and reduced nitrogen species at the individual particle level in the ambient atmosphere, Environ. Sci. Technol. Lett., 8, 9-15, https://doi.org/10.1021/acs.estlett.0c00722, 2020.

Liggio, J., Li, S. M., and McLaren, R.: Reactive uptake of glyoxal by particulate matter, J. Geophys. Res., 110, D10304, https://doi.org/10.1029/2004jd005113, 2005a.

Liggio, J., Li, S. M., and McLaren, R.: Heterogeneous reactions of glyoxal on particulate matter: identification of acetals and 455 sulfate esters, Environ. Sci. Technol., 39, 1532-1541, https://doi.org/10.1021/es048375y, 2005b.

Lim, H. J., Carlton, A. G., and Turpin, B. J.: Isoprene forms secondary organic aerosol through cloud processing: model simulations, Environl. Sci. Technol., 39, 4441-4446, https://doi.org/10.1021/es048039h, 2005.

Ling, Z., Xie, Q., Shao, M., Wang, Z., Wang, T., Guo, H., and Wang, X.: Formation and sink of glyoxal and methylglyoxal in a polluted subtropical environment: observation-based photochemical analysis and impact evaluation, Atmos. Chem. 460 Phys., 20, 11451-11467, https://doi.org/10.5194/acp-20-11451-2020, 2020.

Liu, M., Yu, S., Tian, Z., Xu, Z., and Tong, Z.: Fine particle pH during severe haze episodes in northern China, Geophys. Res. Lett., 44, 5213-5221, https://doi.org/10.1002/2017GL073210, 2017.

Loeffler, K. W., Koehler, C. A., Paul, N. M., and De Haan, D. O.: Oligomer formation in evaporating aqueous glyoxal and methyl glyoxal solutions, Environ. Sci. Technol., 40, 6318-6323, https://doi.org/10.1021/es060810w, 2006.

465 Lutnaes, O. B., Teale, A. M., Helgaker, T., Tozer, D. J., Ruud, K., and Gauss, J.: Benchmarking density-functional-theory calculations of rotational g tensors and magnetizabilities using accurate coupled-cluster calculations, J. Chem. Phys., 131, 144104, https://doi.org/10.1063/1.3242081, 2009.

Ma, F., Xie, H., Li, M., Wang, S., Zhang, R., and Chen, J.: Autoxidation mechanism for atmospheric oxidation of tertiary amines: Implications for secondary organic aerosol formation, Chemosphere, 273, 129207, https://doi.org/10.1016/j.chemosphere.2020.129207, 2021.

470 Malik, M. and Joens, J. A.: Temperature dependent near-UV molar absorptivities of glyoxal and gluteraldehyde in aqueous solution, Spectrochim. Acta. A, 56, 2653-2658, https://doi.org/10.1016/s1386-1425(00)00311-5, 2000.

Marenich, A. V., Cramer, C. J., and Truhlar, D. G.: Universal solvation model based on solute electron density and on a continuum model of the solvent defined by the bulk dielectric constant and atomic surface tensions, J. Phys. Chem. B, 475 113, 6378-6396, https://doi.org/10.1021/jp810292n, 2009.

Marrero-Ortiz, W., Hu, M., Du, Z., Ji, Y., Wang, Y., Guo, S., Lin, Y., Gomez-Hermandez, M., Peng, J., Li, Y., Secrest, J., Zamora, M. L., Wang, Y., An, T., and Zhang, R.: Formation and optical properties of brown carbon from small alpha-dicarbonyls and amines, Environ. Sci. Technol., 53, 117-126, https://doi.org/10.1021/acs.est.8b03995, 2019.

Maxut, A., Noziere, B., Fenet, B., and Mechakra, H.: Formation mechanisms and yields of small imidazoles from reactions 480 of glyoxal with $NH_4(+)$ in water at neutral pH, Phys. Chem. Chem. Phys., 17, 20416-20424, https://doi.org/10.1039/c5cp03113c, 2015.

Munger, J. W., Jacob, D. J., Daube, B. C., Horowitz, L. W., Keene, W. C., and Heikes, B. G.: Formaldehyde, glyoxal, and methylglyoxal in air and cloudwater at a rural mountain site in central Virginia, Journal of Geophysical Research Atmospheres, 100, 9325-9333, 1995.

485 Myriokefalitakis, S., Vrekoussis, M., Tsigaridis, K., Wittrock, F., Richter, A., Br¨uhl, C., Volkamer, R., Burrows, J. P., and Kanakidou1, M.: The influence of natural and anthropogenic secondary sources on the glyoxal global distribution, Atmos. Chem. Phys., 8, 4965–4981, https://doi.org/10.5194/acp-8-4965-2008, 2008.

Nozie`re, B., Dziedzic, P., and Co´rdova, A.: Products and kinetics of the liquid-phase reaction of glyoxal catalyzed by ammonium ions (NH_4^+), J. Phys. Chem. A, 113, 231-237, https://doi.org/10.1021/jp8078293, 2009.

490 Okuno, Y.: Theoretical investigation of the mechanism of the baeyer-villiger reaction in nonpolar solvents, Chem. - Eur. J., 3, 210-218, https://doi.org/10.1002/chem.19970030208, 1997.

Piccot, S. D.: A global inventory of volatile organic compound emissions from anthropogenic sources, J. Geophys. Res., 97, 9897-9991, https://doi.org/10.1029/92jd00682, 1992.

Powelson, M. H., Espelien, B. M., Hawkins, L. N., Galloway, M. M., and De Haan, D. O.: Brown carbon formation by 495 aqueous-phase carbonyl compound reactions with amines and ammonium sulfate, Environ. Sci. Technol., 48, 985-993, https://doi.org/10.1021/es4038325, 2014.

Qian, X., Shen, H., and Chen, Z.: Characterizing summer and winter carbonyl compounds in Beijing atmosphere, Atmos. Environ., 214, 116845, https://doi.org/10.1016/j.atmosenv.2019.116845, 2019.

Raghavachari, K. and Trucks, G. W.: A fifth-order perturbation comparison of electron correlation theories, Chem. Phys. Lett., 157, 479–483, https://doi.org/10.1016/s0009-2614(89)87395-6, 1989.

Sareen, N., Carlton, A. G., Surratt, J. D., Gold, A., Lee, B., Lopez-Hilfiker, F. D., Mohr, C., Thornton, J. A., Zhang, Z., Lim, Y. B., and Turpin, B. J.: Identifying precursors and aqueous organic aerosol formation pathways during the SOAS campaign, Atmos. Chem. Phys., 16, 14409-14420, https://doi.org/10.5194/acp-16-14409-2016, 2016.

Shapiro, E. L., Szprengiel, J., Sareen, N., Jen, C. N., Giordano, M. R., and McNeill, V. F.: Light-absorbing secondary organic material formed by glyoxal in aqueous aerosol mimics, Atmos. Chem. Phys., 9, 2289-2300, https://doi.org/10.5194/acp-9-2289-2009, 2009.

Shi, G., Mahmood, A., Lu, G., Wang, X., Tong, S., Ge, M., Xie, X., and Sun, J.: Adsorption and photodegradation of acetaldehyde and ethylene on TiO_2 (001) surface: experimental and first principle studies, Catal. Lett., 149, 2728-2738, https://doi.org/10.1007/s10562-019-02813-8, 2019.

Shi, Q., Zhang, W., Ji, Y., Wang, J., Qin, D., Chen, J., Gao, Y., Li, G., and An, T.: Enhanced uptake of glyoxal at the acidic nanoparticle interface: implications for secondary organic aerosol formation, Environ. Sci.: Nano, 7, 1126-1135, https://doi.org/10.1039/d0en00016g, 2020.

Surratt, J. D., Lewandowski, M., Offenberg, J. H., Jaoui, M., Kleindienst, T. E., Edney, E. O., and Seinfeld, J. H.: Effect of acidity on secondary organic aerosol formation from isoprene, Environ. Sci. Technol., 41, 5363-5369, https://doi.org/10.1021/es0704176, 2007.

Tuguldurova, V. P., Fateev, A. V., Poleshchuk, O. K., and Vodyankina, O. V.: Theoretical analysis of glyoxal condensation 495 with ammonia in aqueous solution, Phys. Chem. Chem. Phys., 21, 9326-9334, https://doi.org/10.1039/c8cp07270a, 2019.

Volkamer, R., Platt, U., and Wirtz, K.: Primary and secondary glyoxal formation from aromatics: Experimental evidence for the bicycloalkyl-radical pathway from Benzene, Toluene, and *p*-Xylene, J. Phys. Chem. A., 105, 7865-7874, https://doi.org/10.1021/jp010152w, 2001.

Volkamer, R., San Martini, F., Molina, L. T., Salcedo, D., Jimenez, J. L., and Molina, M. J.: A missing sink for gas-phase glyoxal in Mexico City: Formation of secondary organic aerosol, Geophys. Res. Lett., 34, L19807, https://doi.org/10.1029/2007gl030752, 2007.

Wang, S., Du, L., Tsona, N. T., Jiang, X., You, B., Xu, L., Yang, Z., and Wang, W.: Effect of NO_x and SO_2 on the photooxidation of methylglyoxal: Implications in secondary aerosol formation, J. Environ. Sci. (China), 92, 151-162, https://doi.org/10.1016/j.jes.2020.02.011, 2020a.

Wang, Y. , Riva, M., Xie, H., Heikkinen, L., Schallhart, S., Zha, Q., Yan, C., He, X. C., Peräkylä, O., and Ehn, M.: Formation of highly oxygenated organic molecules from chlorine-atom-initiated oxidation of alpha-pinene, Atmos. Chem. Phys., 20, 5145-5155, https://doi.org/10.5194/acp-20-5145-2020, 2020b.

Xia, D., Chen, J., Wang, Y., Xu, T., Su, L., Xie, H., and Allen, D. T.: Organic acid-ammonia ion-induced nucleation pathways unveiled by quantum chemical calculation and kinetics modeling: a case study of 3-methyl-1,2,3-butanetricarboxylic acid, Chemosphere, 284, 131354, https://doi.org/10.1016/j.chemosphere.2021.131354, 2021.

Yang, Z., Tsona, N. T., Li, J., Wang, S., Xu, L., You, B., and Du, L.: Effects of NO_x and SO_2 on the secondary organic aerosol formation from the photooxidation of 1,3,5-trimethylbenzene: a new source of organosulfates, Environ. Pollut., 264, 114742, https://doi.org/10.1016/j.envpol.2020.114742, 2020.

Yu, G., Bayer, A. R., Galloway, M. M., Korshavn, K. J., Fry, C. G., and Keutsch, F. N.: Glyoxal in aqueous ammonium sulfate solutions: products, kinetics and hydration effects, Environ. Sci. Technol., 45, 6336-6342, https://doi.org/10.1021/es200989n, 2011.

Zhao, Y. and Truhlar, D. G.: The M06 suite of density functionals for main group thermochemistry, thermochemical kinetics, noncovalent interactions, excited states, and transition elements: two new functionals and systematic testing of four M06-class functionals and 12 other functionals, Theor. Chem. Account., 120, 215-241, https://doi.org/10.1007/s00214-007-0310-x, 2008.

Ziemann, P. J. and Atkinson, R.: Kinetics, products, and mechanisms of secondary organic aerosol formation, Chem. Soc. Rev., 41, 6582-6605, https://doi.org/10.1039/c2cs35122f, 2012.

Table 1: Estimation of the rates for the oligomerization without and with MA/AM and the growth rates to SOA and BrC under different atmospheric conditions.

Environment	[GL] [a] ppb	k_{rate} [b]			k_{rate}(total) [c]	GR [d]		
		Without MA/AM	With MA	With AM		GR_{SOA}	GR_{BrC}(MA)	GR_{BrC}(AM)
Urban	0.05	2.89×10^{-3}	8.20×10^{-4}	9.10×10^{-4}	4.62×10^{-3} (3.40×10^{-3})	1.41 (1.44)	0.44	0.45
Remote	0.01	5.79×10^{-4}	1.64×10^{-4}	1.82×10^{-4}	9.25×10^{-4} (2.70×10^{-4})	0.28 (0.023)	0.09	0.09
Rural	0.02	1.16×10^{-3}	3.28×10^{-4}	3.64×10^{-4}	1.85×10^{-3} (1.90×10^{-4})	0.57 (0.032)	0.18	0.18

[a] Numbers are the typical measured values of GL from ref (Cerqueira et al., 2003; Lawson et al., 2015; Qian et al., 2019; Munger et al., 1995).

[b] The values are the rates of the oligomerization without and with MA/AM (in s^{-1}).

[c] k_{rate}(total) is the sum of the k_{rate} values without and with MA/AM. And the values in parentheses are from the ref (Liggio et al., 2005a).

[d] The values without and with MA/AM are assumed as the growth rates to SOA and to BrC, respectively. And the values in parentheses are from the ref (Liggio et al., 2005a).

550

555

Figure 1: PES of the GL oligomerization without MA/AM (in kcal mol^{-1}): (a) the initial reactions of GL and (b) the subsequent oligomerization to dimers and trimers. The number denotes the total ΔG_r for each reaction.
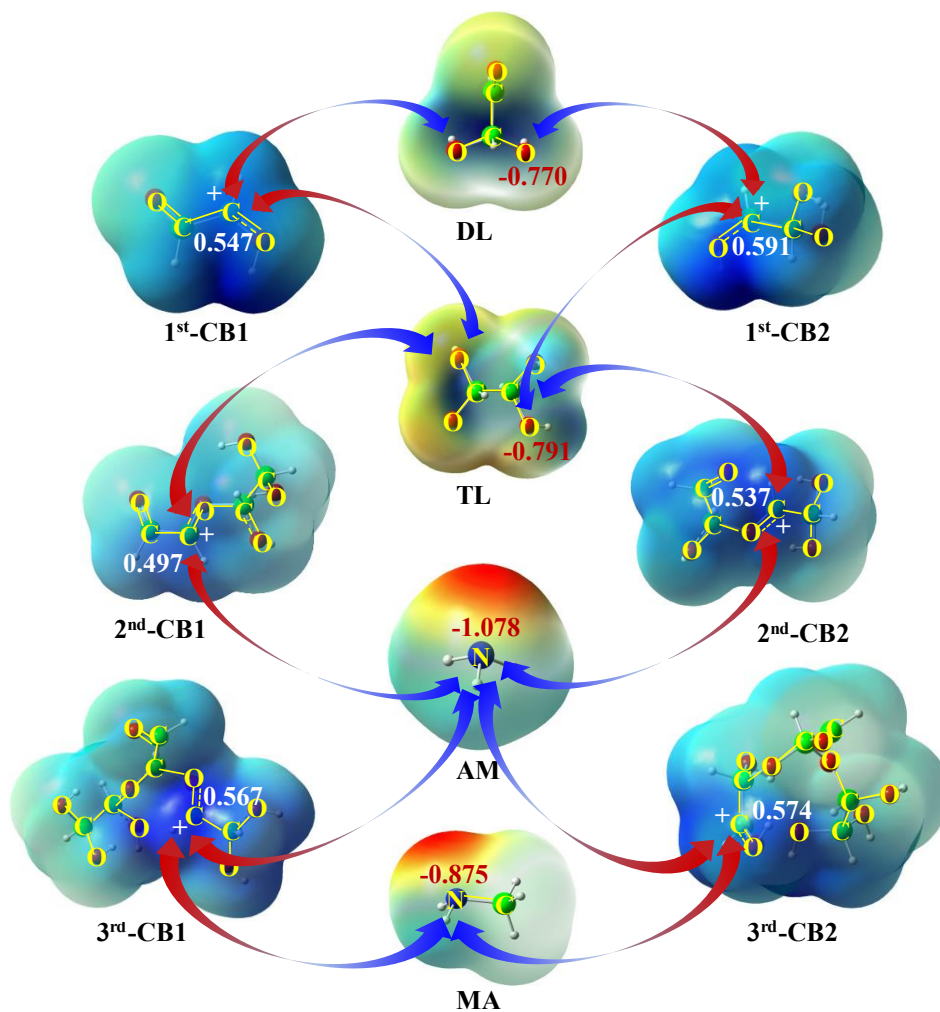
Figure 2: The driving force for oligomerization without and with MA/AM: the natural bond orbitals of DL, TL, MA, AM, and CBs (in e).
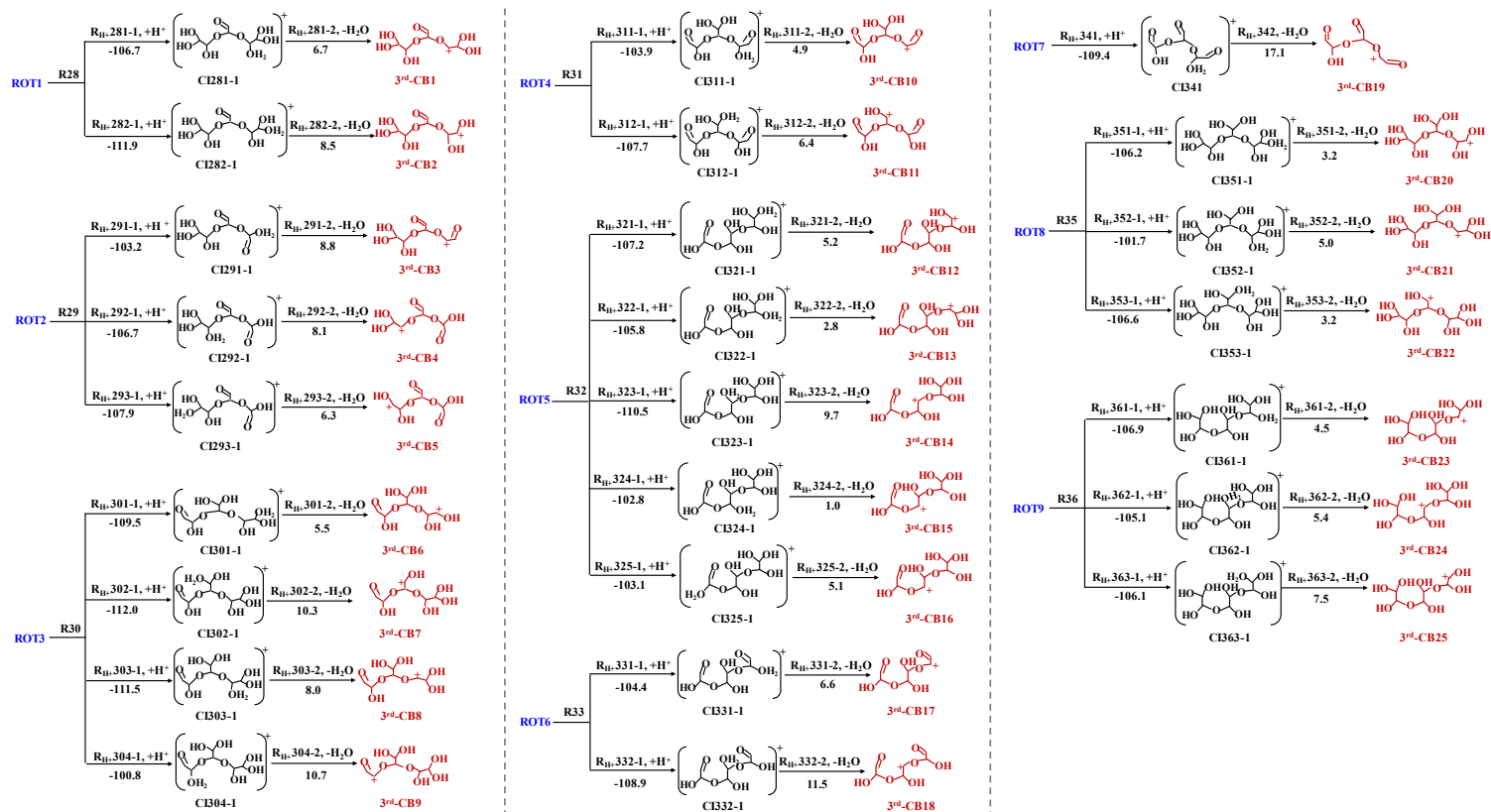
Figure 3: The formation of 3ʳᵈ-CBs from the ring-opening trimers (in kcal mol⁻¹). The value represents the ΔG_r of each step reaction.

565
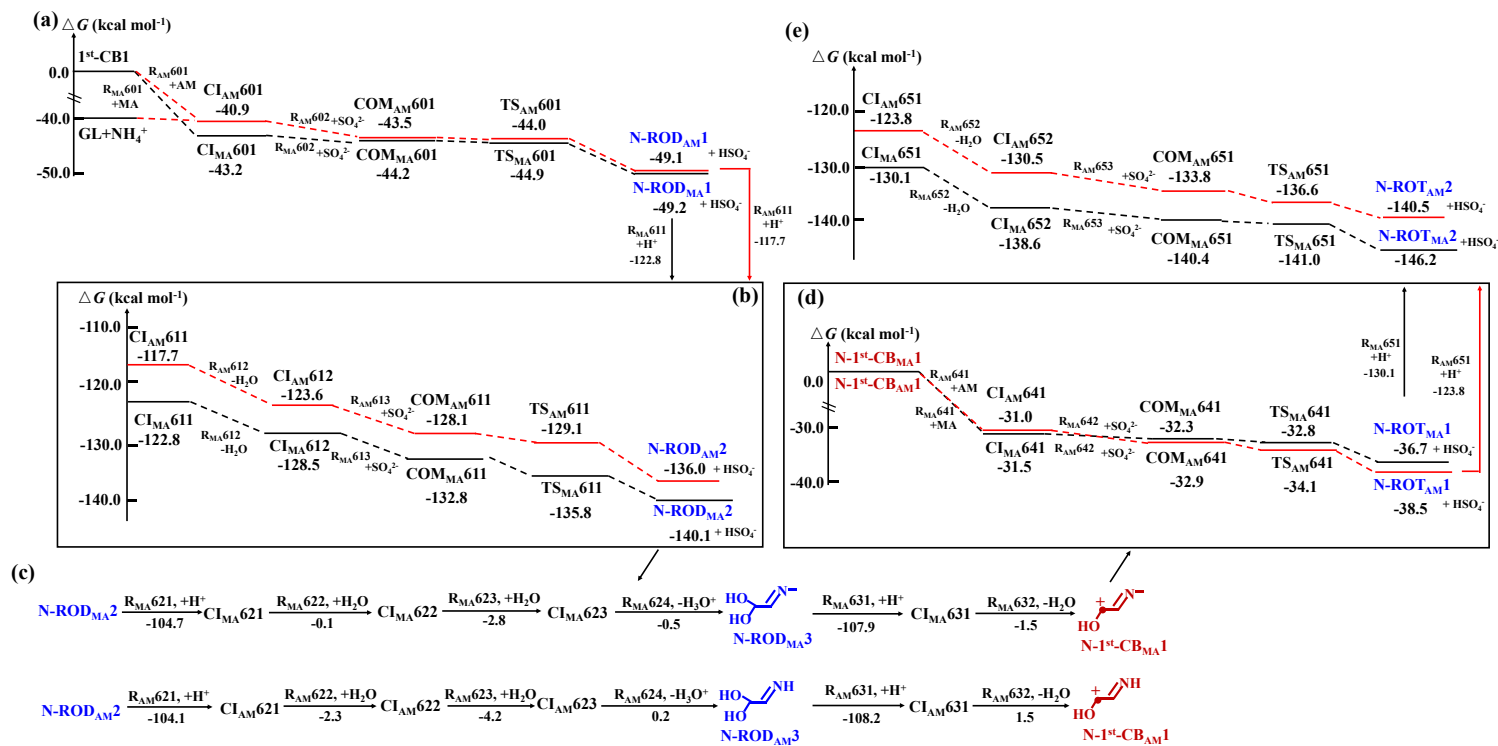
Figure 4: The PES for formation of N-heterocycles starting from (a-b) 1ˢᵗ-CBs with MA/AM to dimers, (c) dimers to N-1ˢᵗ-CBs, and (d-e) N-1ˢᵗ-CBs with MA/AM to trimers (in kcal mol⁻¹). The number denotes the ΔG_r or $\Delta G^{\ddagger}$ for each reaction step, and all energies are relative to the corresponding reactants.

570
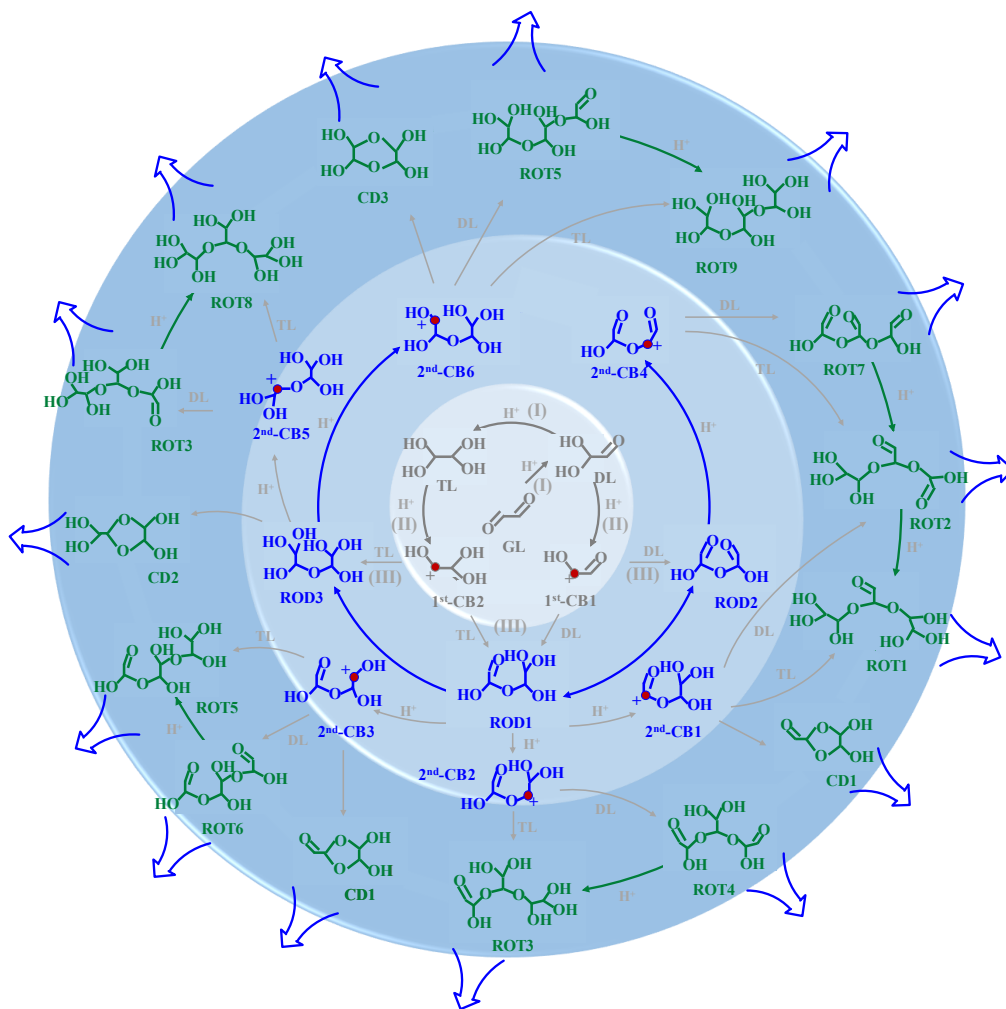
Figure 5: Schematic diagram of formation and propagation of oligomers in the absence of MA/AM. The inside circle ring represents the ion-mediated initial reaction of GL to yield DL, TL and 1st-CBs; The middle circle ring corresponds to the formation of RODs and 2nd-CBs; The outer circle ring denotes the formation and propagation of ROTs from the association reactions of 2nd-CBs with DL/TL.

575